Journal of Electroanalytical Chemistry 799 (2017) 142–155

Contents lists available at ScienceDirect

Journal of Electroanalytical Chemistry

journal homepage: www.elsevier.com/locate/jelechem

Lithium titanate as anode material for lithium ion batteries: Synthesis, post-treatment and its electrochemical response

S. Chauque[a], F.Y. Oliva[a], A. Visintin[d], D. Barraco[b], E.P.M. Leiva[c], O.R. Cámara[a,*]

[a] Departamento de Físico Química, Facultad de Ciencias Químicas, INFIQC-CONICET, Universidad Nacional de Córdoba, Ciudad Universitaria, 5000 Córdoba, Córdoba, Argentina
[b] Facultad de Matemática, Astronomía y Física, IFEG-CONICET, Universidad Nacional de Córdoba, Ciudad Universitaria, 5000 Córdoba, Córdoba, Argentina
[c] Departamento de Matemática y Física, Facultad de Ciencias Químicas, INFIQC-CONICET, Universidad Nacional de Córdoba, Ciudad Universitaria, 5000 Córdoba, Córdoba, Argentina
[d] Facultad de Ciencias Exactas, INIFTA-CONICET, Universidad Nacional de La Plata, 1900 La Plata, Buenos Aires, Argentina

ARTICLE INFO

Keywords:
Lithium-ion batteries
Anode material
Lithium titanate

ABSTRACT

The relationship between the structure and crystallinity of lithium titanate $Li_4Ti_5O_{12}$, at different synthesis post-treatment conditions on the electric energy storage capacity is discussed. $Li_4Ti_5O_{12}$ was synthesized by solid-state reaction at a high temperature and time (950 °C, 24 h) and the resulting material was post-treated with a ball milling process at different times. Additional samples were prepared with a post-calcination after and adding graphite carbon previously to the longer applied ball-milling time. All the obtained materials were structurally and morphologically characterized by XRD and SEM techniques. To study the effect of ball milling time on the lithium-ion storage capacity, electrochemical experiments of galvanostatic charge-discharge cycling, cyclic voltammetry, and rate capability experiments were performed. The application of high-energy milling showed that the obtained specific capacity increased with particle size reduction as long as the crystallinity degree of the LTO material remained high. The Li-ion diffusion coefficient for each material was obtained, as well as its specific resistivity and the intrinsic rate constant for the electrochemical process. It was possible to observe that the ball-milling treatment producing improvements in the charge storage capacity leads also to improvements in mass transport and electrical conduction, although not necessarily produce better electrochemical kinetic behavior. The inter-particle connectivity was analyzed in terms of state-of-the-art percolation modeling.

1. Introduction

In recent years, the use of renewable energy resources as well as more efficient energy storage systems have been favored topics on the agenda of most influential governments and international organizations. A more sustainable energy system is urgently required by modern society due mainly to global warming effects, the fluctuating price of oil, and contamination produced by fossil fuel combustion. This situation has driven, within the area of scientific investigation, a search for improved electrochemical storage systems that can safely store energy from sustainable sources, such as wind and solar power, and also provide the energy needed, for example, for transportation and residential uses.

The use of portable electronic devices has been made feasible thanks to the technology of lithium-ion batteries (LIB). These were first commercialized by Sony in 1991, and consisted of a graphite anode and a layer oxide cathode, which are still widely used today. The energy storage capacity of the LIB system is 5 times higher than that of lead-acid batteries, and has an average voltage of 3.8 V per cell in comparison with the lower average of 2.0–2.2 V of the lead-acid batteries [1].

LIB also have the advantage of lower weight, higher energy density and faster charge and discharge rates, compared to other similar technologies. However, even though they are the most widely used batteries in portable electronics, it is important to address several issues regarding their safety, and to improve further the energy storage capacity in order to be used in electric vehicles, which are predicted to replace those with internal combustion engines in the near future. Since graphite has a fragile structure and incorporates lithium at a similar potential to that of lithium metal deposition, the use of better and safer anodes is necessary [2,3]. Related to this, the Lithium titanate $Li_4Ti_5O_{12}$ (LTO) is currently one of the best candidates for anode materials of

* Corresponding author at: Departamento de Físico Química, Facultad de Ciencias Químicas, Universidad Nacional de Córdoba, Ala 1, Pabellón Argentina, Ciudad Universitaria, 5000 Córdoba, Argentina.
E-mail address: ocamara@fcq.unc.edu.ar (O.R. Cámara).

http://dx.doi.org/10.1016/j.jelechem.2017.05.052
Received 25 January 2017; Received in revised form 2 May 2017; Accepted 29 May 2017
Available online 30 May 2017
1572-6657/ © 2017 Elsevier B.V. All rights reserved.

SEL 2007
Amperex v. SEL
IPR2023-01349

safer LIB for various reasons: Firstly, the lithium insertion process takes place at a higher potential than in graphite, thereby minimizing the decomposition of the solvent employed and consequently avoiding the formation of a solid electrolyte interface (SEI). Also, LTO is a "zero-strain" material with only a 0.2% of change in unit cell volume when Li^+ ions are intercalated or de-intercalated [4] and has a prolonged lifetime in charge/discharge cycling. These aspects counterbalance the two main disadvantages of this material, namely, its lower output in voltage compared with currently used graphite materials (of about 1.5 V vs Li^+/Li^0) and also its lower theoretical specific capacity (175 vs 372 mAh/g). The first of the LTO disadvantages is inherently thermodynamic in essence and it is not possible to overcome. The second is that the spinel structure of $Li_4Ti_5O_{12}$ accepts only three additional Li^+ ions in structural positions similar to that occupied by Ti^{4+} ions in order to obtain the rock-salt structure, where the total number of cations equals that of the anions [5] and represent the higher possible state of lithiation energetically favorable. So, the current research trends focus on synthesizing LTO materials through diverse methods being the ceramic, sol-gel and hydrothermal routes the most simple and scalable to industrial production, and on optimizing the practical performance and kinetic response to high applied currents through an adequate control of the LTO particle size, morphology and connectivity. Even though LTO and other related materials, such as rutile or anatase TiO_2, TiO_2-B and hydrogen titanates, have been extensively studied and characterized as lithium storage material, other families of related compounds, for example, sodium titanates or doped alkaline titanates, have received less attention [6–11]. In the current study, we focused on the synthesis of LTO by a solid-state method and investigated the effects of a mechanical post-treatment of this material aimed at decreasing the particle size, on the electrochemical behavior and its response in the lithium insertion-desinsertion process. Among the several synthesis methodology reported in the literature, including hydro- and solvothermal, sol-gel, solution and combustion, spray pyrolysis and microwave-assisted processes among others, the solid-state or ceramic method offer several advantages such as the low cost and abundance of the reactants and the high purity of their product; it is highly reproducible, simple and easy to conduct and to scale-up. These are very relevant aspects from the technological point of view despite this method being also highly energy and time consuming. In this work, we analyze several relevant electrochemical parameters and correlate them with the particle size and crystallinity of the active LTO material, besides the gravimetric specific capacity and rate capability behavior usually and only reported in the current literature.

2. Experimental

2.1. Active material synthesis

$Li_4Ti_5O_{12}$ was prepared by a solid-state method, where lithium carbonate (Li_2CO_3) and titanium dioxide (TiO_2 anatase) were used as raw materials. The reagents were mixed at a stoichiometric ratio for 20 min in an agate mortar (AM), with acetone added to favor the mixing process. Afterwards, the mixture was annealed applying a heating ramp of 2 °C/min from ambient temperature to 950 °C over 24 h. After the annealing process a cooling ramp was set at 5 °C/min [12]. The overall equation of the synthesis reaction can be expressed as follows:

$$5\ TiO_2 + 2\ Li_2CO_3 \rightarrow Li_4Ti_5O_{12} + 2\ CO_2 \quad (1)$$

After the synthesis, a coarse white powder was obtained and ground in an AM. Furthermore, milled samples were prepared by ball milling of the LTO synthesized under an air atmosphere. The milling process was carried out in a planetary ball mill (Fritsch PULVERISETTE 7 premium line) with a hard metal tungsten carbide grinding bowl and zirconium oxide balls (10 mm in diameter), with a ratio of the ball mass to powder of 22:1. The milling was carried out at a speed of 300 rpm, which was programmed with 10 min of milling followed of a pause of 10 min in order to prevent excessive heating. Total milling times of 30, 60 and 90 min were applied, and the obtained samples were named LTO-W (corresponding to the LTO without ball milling post-treatment), BM30, BM60 and BM90, according to the ball milling time (where BM stands for ball milled).

According to the obtained experimental results with the above mentioned samples (discussed in the following sections), two other types of samples were prepared with the highest BM time (90 min) in order to: a) correct the impact of the high energy milling process on the crystallinity of the smaller particles, and b) get a better inter-particle connectivity. These samples were prepared as follows:

a) A BM90 sample was post-treated applying an additional heating ramp at 2 °C/min from the ambient temperature up to 800 °C and maintaining this temperature for 8 h. Then, a cooling ramp was set at 5 °C/min, and the resulting sample named BM90-PA (PA for post annealed).
b) A hybrid carbon-LTO material was prepared using the ball milling technique on a mixture of the LTO-W sample and graphite carbon (at a ratio of 90:10 in mass). This mixture was ball milled for 90 min as previously described and named BM90-G (where G stands for graphite hybrid). The graphite carbon used to prepare this sample was graphite flakes from Sigma-Aldrich (CAS 7782-42-5), with particle size of 150 μm or less.

All the prepared samples were kept in a humidity-free ambient before use.

2.2. Structural characterization

The crystalline structure of the samples was analyzed by X-ray diffraction (XRD) using Cu Kα radiation (λ = 1.5418 Å), and measured with a PANalytical X'Pert PRO diffractometer. The XRD patterns were obtained in the 2θ range from 10° to 90°, with 0.02° steps and a counting time of 10 s. The crystalline structures were identified using High Score software, with the Rietveld structure refinements of the XRD patterns being performed using the FULLPROF program and the Inorganic Crystal Structure Database (ICSD).

The surface microstructure of the samples was examined by Scanning Electron Microscopy (SEM) in a FE-SEM Σigma Microscope, using an accelerating voltage of 8 kV at a working distance of 8.5 mm with a secondary electron detector.

2.3. Electrochemical characterization

Three-electrode T-cells (Swagelok type) were assembled and used for all electrochemical measurements. The working electrodes were prepared using a mixture of the active material (LTO-W, BM30, BM60, BM90, BM90-PA and BM90-G), polyvinylidene fluoride (PVDF) as a binder and conductive carbon black (Timcal Super P) to increase electrical conductivity, at a weight ratio of 80:10:10, respectively. These mixtures were dispersed in *N*-methyl-2-pyrrolidinone solvent and maintained in agitation for 12 h to assure a homogeneous dispersion. Copper foils 15 μm in thickness were coated with the resulting slurries, dried in an oven at 80 °C for 24 h and pressed by applying 10 ton/cm^2. The total mass of the film coatings was approximately 1 mg/cm^2. The coated foils were punched into 8 mm diameter disks to obtain the working electrode, and dried at 80 °C overnight under vacuum before being placed in the glovebox for cell assembling.

Metallic lithium was used both as a reference and for counter electrodes (8 mm diameter disks), with fiberglass disks being used as spacers between the three electrodes. All the potential values reported hereafter are referred to the Li^+/Li^0 couple standard potential. The working solution consisted of ethylene carbonate (EC) and dimethyl-carbonate (DMC) solvent mixture (1:1 by mass) containing 1 M $LiPF_6$

salt as the electrolyte. The electrode cells were assembled inside a glovebox chamber (MBraun MB10 compact) in an Ar atmosphere with a concentration of O_2 and H_2O of less than 0.5 ppm. Unless otherwise specified, the chemicals were obtained from Sigma-Aldrich without further purification. All electrochemical measurements, such as galvanostatic charge-discharge (GCD) cycles, cyclic voltammetry (CV), and rate capability (RC) experiments, were carried out using a Gamry Potentiostat-Galvanostat at room temperature.

For each active anode material, ten GCD cycles were performed at a current of 0.5C within the interval 3.0 to 1.0 V to analyze the specific capacity of the different synthesized LTO active materials, expressed as mAh/g (in terms of LTO mass). The theoretical capacity (according to the deposited mass in the electrode) was used in order to make a first estimate of the current to initiate the experimental evaluation of the material, but the actual C current value was obtained experimentally for each material. In order to determine the experimental C current value a preliminary GCD experiment was conducted at a current value such that the LTO mass actually existent in the coating of the electrode was charged/discharged in 1 h according to the theoretical specific capacity. From this first experimentally obtained time of charge-discharge value, it was determined the actual 1C current value. The absolute current values for C were 68.5, 76.7, 85.7, 79.4, 38.8 and 154.8 mA/g for LTO-W, BM30, BM60, BM90, BM90-PA and BM90-G samples, respectively. The CV experiments were performed with each electrode at different scan rates of between 0.5 and 5.0 mV/s, which was within the previously mentioned voltage range. Finally, RC experiments were performed with the same cut-off potentials as the GCD cycles, applying a charging current of 0.5C while the discharging currents were set at 0.5C, followed by 1C, 2C, 5C, 10C and then 0.5C, again. At each C rate applied, 10 cycles of charging/discharging were performed.

3. Results and discussion

3.1. Structural characterization

Fig. 1(a) shows the XRD pattern of LTO-W, which presents the typical peaks of ICSD # 75711 for the $Li_4Ti_5O_{12}$ compound. Rietveld refinement for the XRD pattern revealed a face-centered cubic structure with a space group of *Fd3*m (lattice parameter = 8.3547(4) Å). Peaks related to possible impurities remaining from the precursors in the synthesis procedure, such as rutile TiO_2 or a pure phase of Li_2O, were not observed. From the parameters obtained from the refinement process, a crystal structure representation for $Li_4Ti_5O_{12}$ is shown in Fig. 1(b), where the *b* axis is coming out of the plane (it can be noted that the structure observed along the *a* and *c* axes are the same). Continuous tunnel channels can be observed along the three axes, in between four oxygen ions (marked with a black circle in the figure) that may provide a possible Li^+ ion pathway for diffusion into the matrix structure. Due to the face-centered cubic structure, the Li^+ ions can be inserted in any direction, resulting in an isotropic effect that might result in the practical possibility of achieving the theoretical storage capacity for this material, in contrast with other types of alkali titanates, such as the sodium titanates $Na_2Ti_3O_7$ and $Na_2Ti_6O_{13}$, where channels in only one direction were observed [12].

One unit formula of $Li_4Ti_5O_{12}$ has the capability of an electrochemical and reversible uptake of up to three lithium ions, which delivers a theoretical capacity of 175 mAh/g and obtains $Li_7Ti_5O_{12}$ with a rock salt structure. This phase transformation, from the spinel to the rock salt structure, results in a slight decrease of the lattice parameter, with only a 0.2–0.3% change in the cell volume (from 8.364 to 8.353 Å, according to experimental data of Sun et al. [13]). It is interesting to note that the impossibility of adding two other Li^+ ions in the unit formula, corresponding to the full reduction of the five Ti ions from 4 + to 3 + formal oxidation state, is due to the lack of adequate interstitial sites to locate the Li^+ ions. However, Shu and Ge et al. have stated that this additional lithiation can be achieved near 0 V vs Li^+/Li^0 [14,15], in spite of the fact that at this experimental condition the formation of an SEI is favored.

Fig. 2 shows the XRD patterns for all the LTO substrates prepared, with LTO-W, BM30, BM60, BM90 and BM90-PA corresponding to (a) to (e), respectively. All the patterns were represented with the same full scale of intensity in order to analyze any changes in the crystallinity due to the post-treatment procedure on the materials. Considering that the patterns were recorded on the same mass amount and with the same exposition time for all the samples, the peak height (in relative terms) can be correlated with the crystallinity condition of the sample. For this, we have chosen the diffraction peak of the (111) plane due to its high intensity, and the peak height of the LTO-W sample as reference (considering that this sample was the starting point for the subsequent treatments). As the milling time increased, the XRD patterns (a) to (d) show a significant decrease in the intensity and an increase in the broadening of most of the Bragg peaks (positions included in Fig. 2(a)), indicating an increased disorder of the lithium titanate structure. The

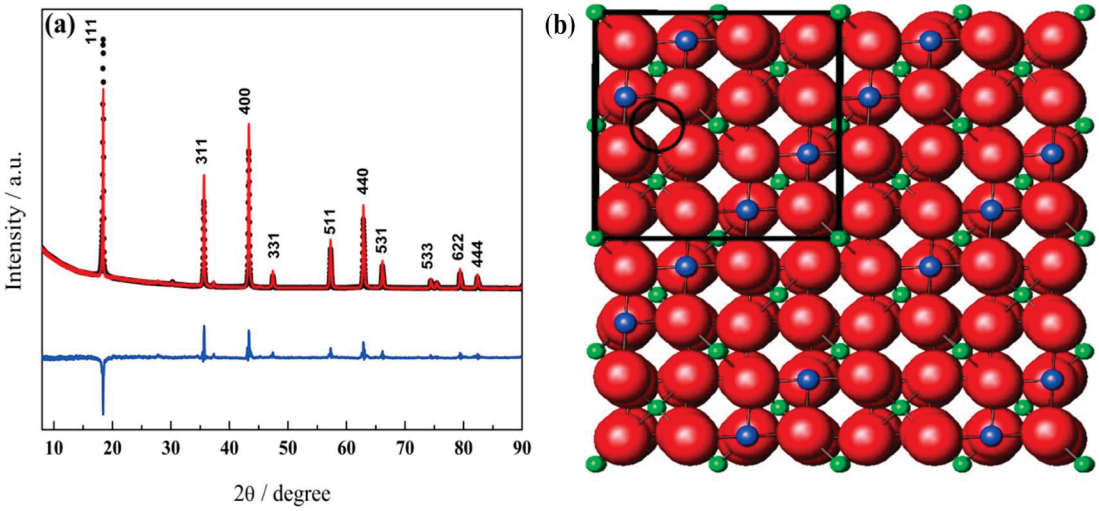


Fig. 1. (a) XRD pattern of the LTO-W (black points) and Rietveld fitting (red line). The difference curve is shown underneath the pattern (blue line). (b) Representation of the schematic structure for $Li_4Ti_5O_{12}$, reconstructed from the atoms positions obtained by Rietveld analysis. The *b* axis is coming out of the plane and four replicated unit cells in the *a*-*c* plane are shown. The black frame corresponds to the unit cell. Colour code: blue: titanium, red: oxygen and green: lithium. (For interpretation of the references to colour in this figure legend, the reader is referred to the web version of this article.)

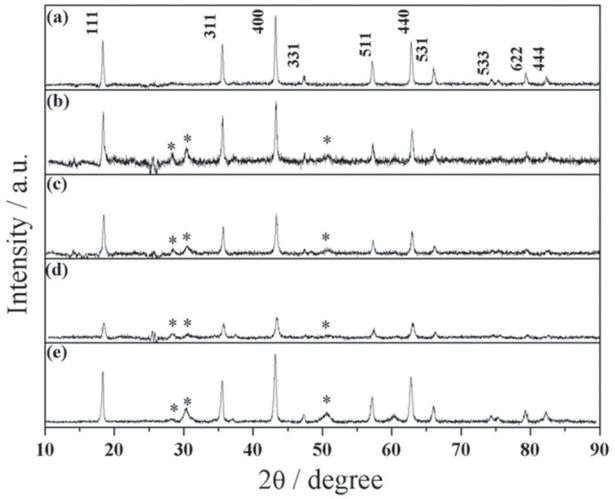


Fig. 2. XRD patterns of the prepared lithium titanate samples (a) LTO-W, (b) BM30, (c) BM60, (d) BM90 and (e) BM90-PA. All patterns are shown with the same full scale in intensity. The diffraction peaks marked with asterisk correspond to zirconia phases.

diffraction peaks marked with asterisk correspond to zirconia phases, coming from the balls material of the ball mill. Hence, it can be concluded that as the milling time increases, the crystallinity of the LTO samples decreases and it is transformed into a more amorphous material. It is interesting to observe that an annealing stage applied after the extensive ball milling of 90 min (XRD pattern (e), corresponding to the sample BM90-PA) recovered a high crystallinity degree for the LTO compound.

SEM images of all the prepared LTO samples were obtained from the film coating deposited on the copper foil (containing the active LTO material, binder and carbon particles) and previous to any electrochemical experiment, in order to obtain an actual picture of the initial state of the electrode material (Fig. 3). It is observed that the post-treatment of the starting material strongly influenced the resulting final particle size. As the milling time increased, the particle size decreased considerably, leading to a greater specific surface area. This is an interesting property to aim at in anodes for LIBs, since a small particle size might improve Li^+ ion insertion in the host matrix and provide an excellent surface area/mass ratio for the active material. The particle sizes obtained from the SEM images using the program *ImageJ* are shown in Table 1. This program indicates the projected 2D surface area for the analyzed LTO particles, and then assuming a spherical geometry, the diameter for the particle can be estimated. The distribution of the particles of LTO active material and the conductive carbon was homogeneous through the entire film surface, as it is observed in Fig. A.1 of the Appendix, where it is shown the distribution condition of titanium and carbon, obtained by Electron Probe Micro-Analysis in the LTO-W, BM30, BM60 and BM90 samples, together with a SEM micrograph of each one. The same homogeneous distribution was observed along the thickness of the film (figure not shown).

Milling times lower than 30 min (results not shown) did not reveal any significant particle size differences with respect to the unmilled sample (LTO-W). It can be observed that the annealing step following the higher ball milling time (sample BM90-PA) produced a sinterizing effect that increased the final particle size, leading to a size similar to that of the non-ball milled sample (LTO-W). In contrast, the presence of graphite mixed with lithium titanate previous to the ball milling process produced a larger particle size than that resulting from using the same milling time without graphite. In the present work, the BM90-G sample was similar in particle size to that of the BM60 sample. This result might be attributed to the known softness of the graphite carbon having a milder effect on the high energy milling process. Fig. 4 shows the changes in both particle size and the relative intensity of the XRD peak (111), with the sample treatments.

3.2. Electrochemical analysis

In order to study the electrochemical performance in the storage capacity of the different substrates prepared as active anode material, GCD curves were obtained at 0.5C in the voltage interval of 3.0 to 1.0 V. The charge/discharge curves corresponding to the first and 10th cycles for all electrodes studied are shown in Fig. 5(a), where the specific capacities reported refer to the LTO mass in the electrode coating. Hereinafter, all the discussions will be referred to the 10th cycle, considering that it correspond to the stabilized response of each electrode material. In all cases, a flat plateau can be observed at approximately 1.55 V, which is characteristic for the two-phase reaction based on the Ti^{4+}/Ti^{3+} redox inner couple [12]. The specific capacity for electrodes prepared with LTO materials milled at intermediate times (between 5 and 30 min) did not reveal any relevant differences with respect to the LTO-W electrode (data not shown). In addition, the electrode prepared with 60 min of milling presented the highest specific capacity (approximately 145 mAh/g). Surprisingly, the electrode with the highest milling time (90 min) had the lowest capacity, which was even lower than for the untreated material (with hand-milling only using an agate mortar).The excellent electrochemical reversibility in the charge-discharge process was noteworthy for all the prepared materials, as evidenced by the low potential difference between the corresponding plateaus (30–50 mV), measured at the middle point of the cycle and depending on the active material. The cycling performance of all the electrodes tested at 0.5C revealed a great stability of these active materials, as displayed in Fig. 5(b), where the missing points correspond to the other electrochemical experiments performed, which were each considered to be equivalent to one GCD cycle, namely five CV cycles (cycles 11 to 16), one EIS experiment (cycle 18) and 41 RC measurements (cycles 40 to 80).

The last ten charge/discharges cycles (of a total of 80 cycles) for all electrodes, except BM90, presented a practically unchanged value of specific capacity with respect to the first ten cycles, thus demonstrating the excellent cyclability performance of these active materials.

In order to investigate the reasons for the reduction in specific capacity at higher milling times, GCD experiments were performed on samples prepared with an annealing treatment after the ball milling for 90 min (BM90-PA) and with the hybrid material composed of LTO and graphite ball milled for 90 min (BM90-G). Fig. 6 shows the GCD curves for BM90-PA and BM90-G samples, with the BM90 sample included as a reference data. Taking into account that milling for 90 min decreased the crystallinity of the LTO material and that the thermal treatment up to 800 °C recovered this (as was shown in Fig. 2(e)), then recovery of the electrochemical behavior would be expected after the thermal treatment. However, the electrochemical behavior did not show an improvement in the GCD curve for the BM90-PA material (instead, a reduction in the specific capacity was observed). This experimental result might seem unexpected, considering that the presence of a highly ordered crystalline structure in the LTO material must be a key feature in the lithium ion insertion. In contrast, the marked increase observed in the particle size by sinterization appeared to be responsible for its lower specific capacity response, whereas the hybrid material BM90-G revealed the highest specific capacity (normalized by LTO mass) of all the prepared samples. The addition of graphite particles previous to the ball milling stage resulted in an increase in specific capacity of approximately 87%, with respect to the same milling time without graphite. However, the average particle size observed with BM90-G was similar to that of the BM60 sample (which showed the highest specific capacity without post-treatment after ball milling). Both the BM60 and BM90-G samples revealed similar specific capacities, which corresponded to about 83–86% of the maximum theoretical capacity for the LTO material, respectively. From the above discussion, we conclude

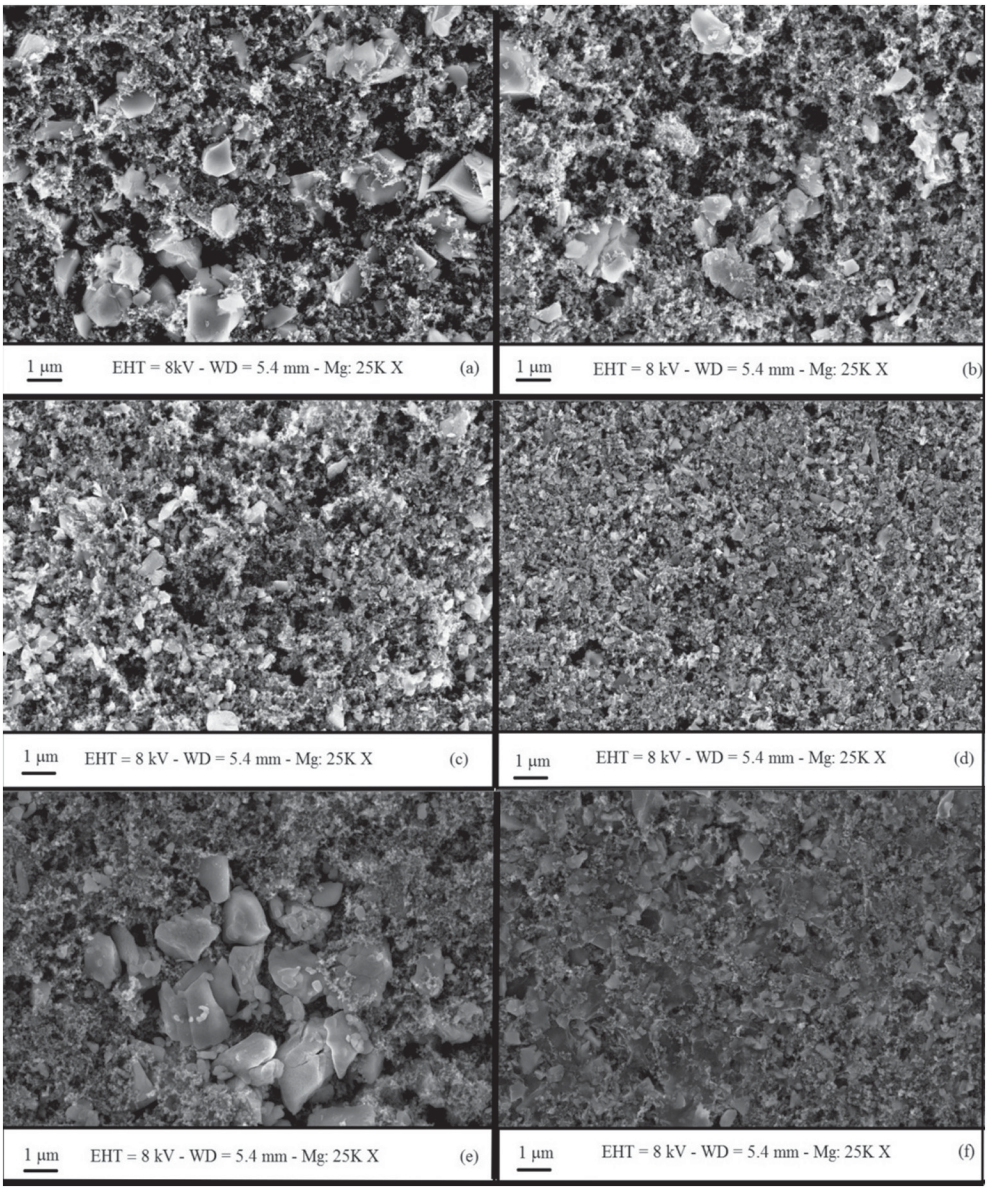


Fig. 3. SEM images for each electrode material deposited on the Cu foil and previous to any electrochemical experiment: (a) LTO-W; (b) BM30; (c) BM60 and (d) BM90, (e) BM90-PA and (f) BM90-G. Magnification bar: 1 μm.

that the decrease in particle size produced an increment in the anode specific capacity until the particle size was too small to maintain an efficient inter-particle connection. This point will be further analyzed below in the context of theoretical work. Summing up, the loss of conductivity was prevented and the crystallinity was maintained by the addition of graphite during the ball milling process.

In Fig. 7 it is shown the effect of prolonged and continuous GCD cycling at 0.5C performed on the electrodes that produced the best behavior in the previous experiments, which were the BM60 and BM90-G LTO materials. The cycling was sustained up to 100 cycles from the

Table 1
Average particle size estimated from SEM images (Fig. 3) using *ImageJ* program.

Sample	Average particle size/μm
LTO-W	1.01
BM30	0.94
BM60	0.62
BM90	0.36
BM90-PA	1.13
BM90-G	0.62

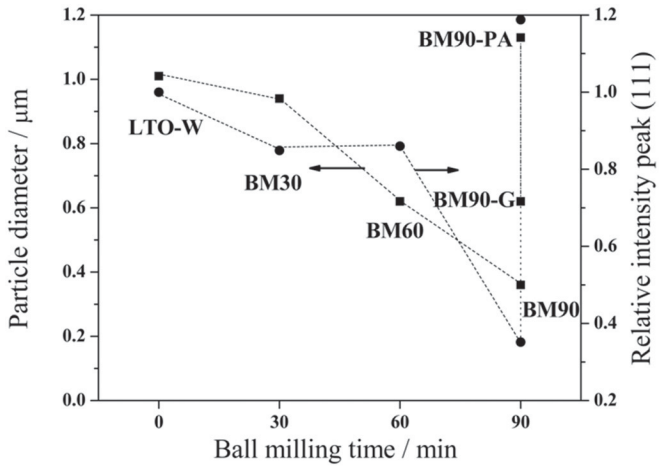


Fig. 4. Particle diameter (obtained from SEM images) (square) and relative intensity of the DRX peak (111) in respect to the LTO-W sample (circle) as a function of the ball milling time.

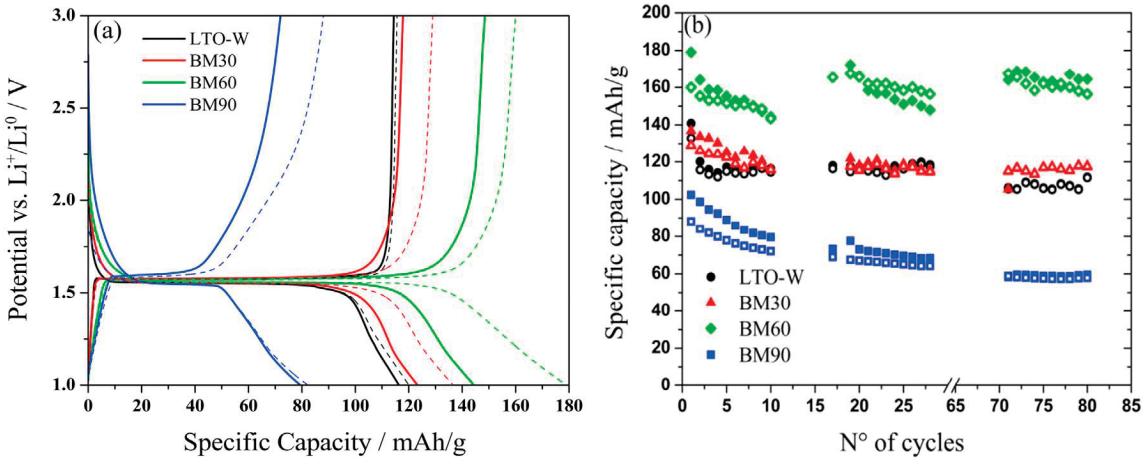


Fig. 5. GCD results obtained at 0.5C for all the active material electrodes: (a) GCD curves corresponding to the first (dashed line) and 10th (solid line) cycles. (b) Cycling stability (specific capacity vs. number of cycles) for LTO-W (black), BM30 (red), BM60 (green) and BM90 (blue). Full symbols correspond to the charge and empty symbol to the discharge process, respectively. (For interpretation of the references to colour in this figure legend, the reader is referred to the web version of this article.)

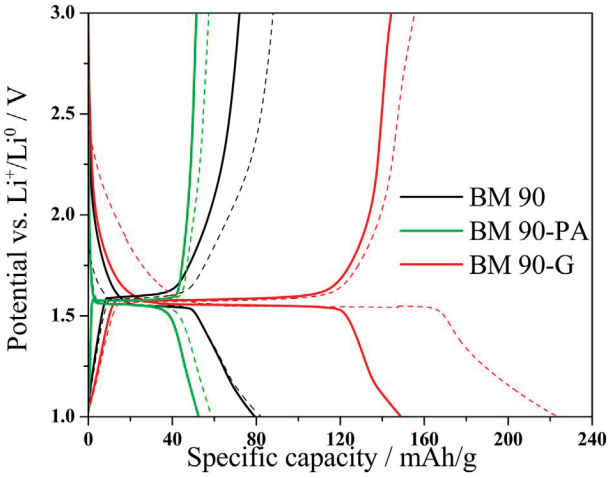


Fig. 6. GCD curves corresponding to the first (dashed line) and 10th (solid line) cycles for the samples BM90 (black line), BM90-PA (green line) and BM90-G (red line). (For interpretation of the references to colour in this figure legend, the reader is referred to the web version of this article.)

initial stabilized response of these electrodes (obtained after the first few cycles). For both samples the coulombic efficiency in each individual charge/discharge cycle was 100% and a loss in specific capacity of about 12 and 4% for MB60 and MB90-G samples, respectively, was observed. Clearly, these LTO materials show a very good cyclability.

Fig. 8 shows CV profiles for all the samples studied in this work. The peak potential of the Ti^{4+}/Ti^{3+} redox couple observed at the lowest scan rate corresponded well with the insertion potential of the GCD curves for each electrode. When the scan rate was increased, the cathodic current peak shifted towards lower potentials and the anodic current peak to higher potentials, as expected from the theoretical framework of cyclic voltammetry. This overall behavior indicates that at higher scan rates the redox process became more irreversible, and did not permit the processes of insertion/de-insertion of Li^+ ions into the host matrix to be fully completed. Furthermore, as the milling time increased, the CVs curves showed a more irreversible behavior, which may have been due to the poor crystallinity of the obtained material. From the particular characteristics observed in the CV profiles observed at increasing scan rates and for different synthesized samples, several interesting features can be described.

For all samples, the difference between the potentials of the anodic and cathodic current peaks, defined as $\Delta E_{peak} = E_{peak}{}^{an} - E_{peak}{}^{cath}$,

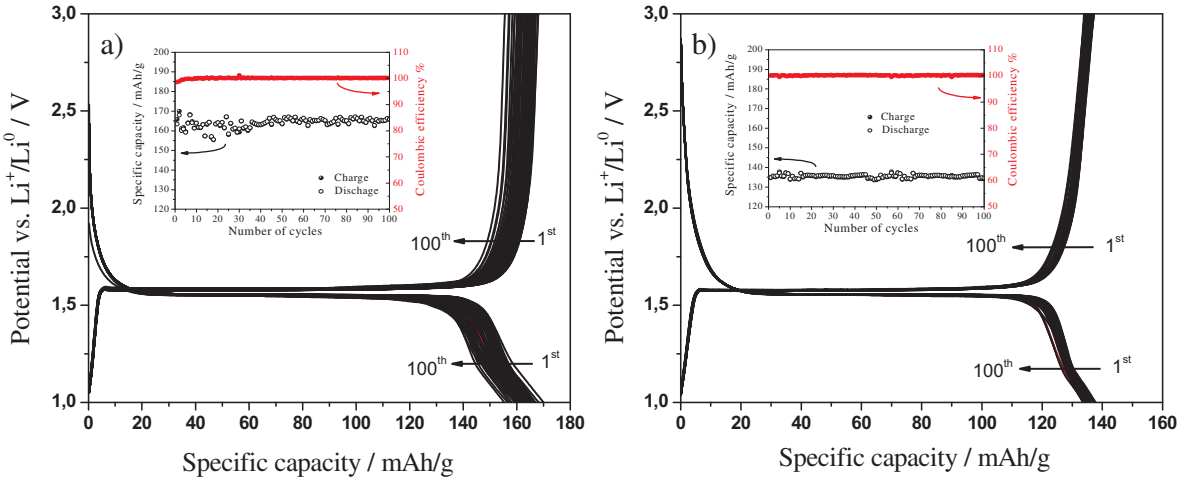


Fig. 7. GCD curves corresponding to a prolonged cycling (100 cycles) performed at a rate of 0.5C for: a) BM60 and b) BM90-G samples (the arrows show the direction of change). In the insert it is shown the coulombic efficiency in each individual charge/discharge cycle and the specific capacity as a function of the number of cycles.

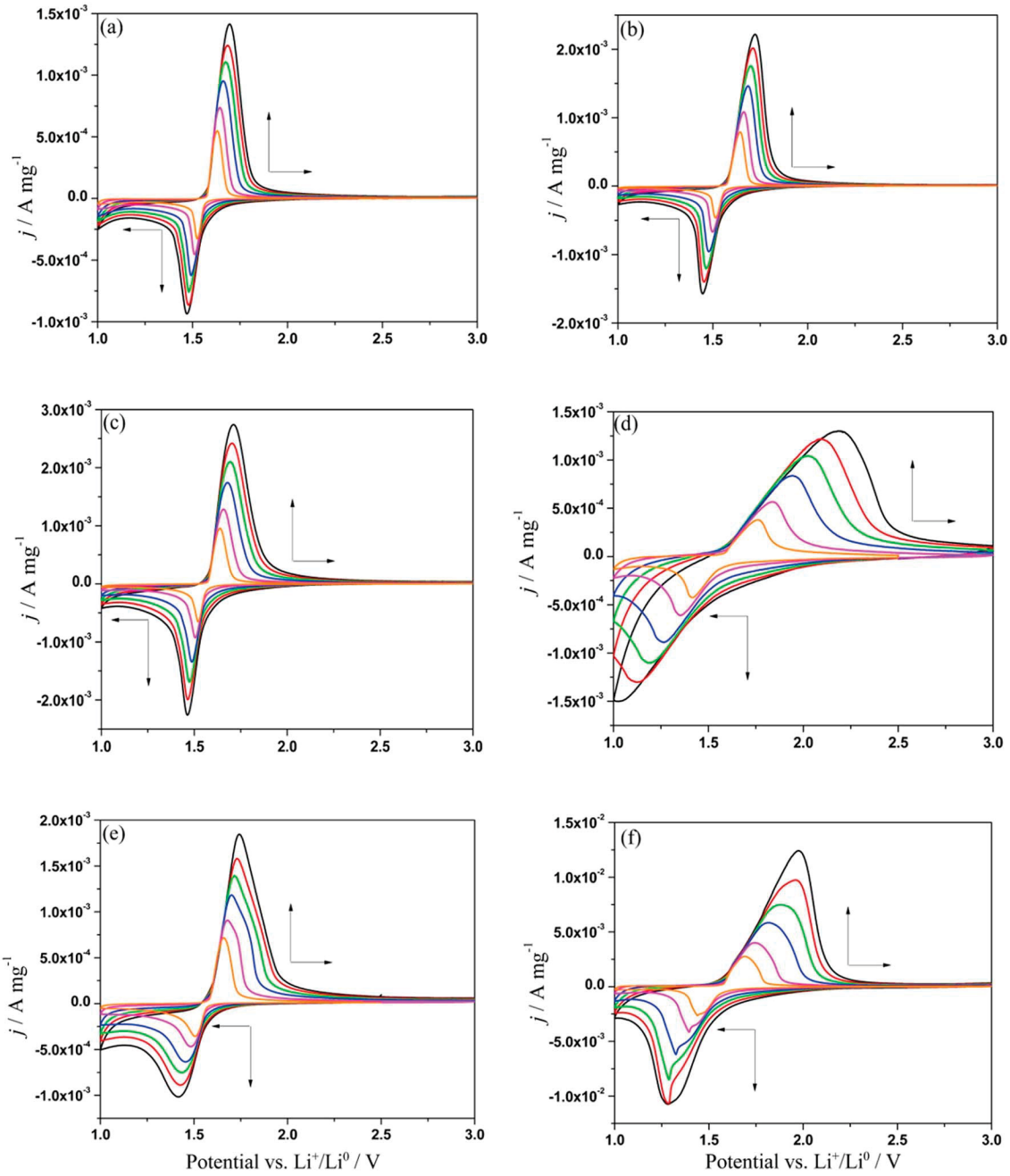


Fig. 8. CV curves at different scan rates (0.5, 1.0, 2.0, 3.0, 4.0, and 5.0 mV/s) between 1.0 and 3.0 V vs Li^+/Li^0, of (a) LTO-W, (b) BM30, (c) BM60, (d) BM90, (e) BM90-PA and (f) BM90-G. In these figures the current was normalized by the mass of the active material (*j*, in A/mg) present in each sample. Arrows in the figures indicate the direction of the changes in *j-E* profiles according to the scan rate increment.

increased linearly with the square root of the scan rate ($v^{1/2}$) (as shown in Fig. 9(a), with regression factors in the linear fit by the least square method between 0.970 and 0.990), a feature that is characteristic of a quasi-reversible electrochemical charge transfer process [16]. Each sample had a different slope, something that is reasonable considering that this is inversely dependent on the standard heterogeneous rate constant (k^0) of the charge transfer process [16]. Fig. 9(b) shows the variations of the slope (ΔE_{peak} - $v^{1/2}$) with the milling treatment, where a slow increase for the lower ball milling times and a sharp increase for the longest time can be observed. The higher values of the slope (ΔE_{peak} - $v^{1/2}$) represent lower values for the k^0 parameter, thus indicating a slower kinetic for the lithiation/de-lithiation process. Despite ball milling for 90 min, an annealing treatment post-milling or a milling with graphite added produced a better kinetic behavior.

In order to understand the kinetic behavior of the active materials, the current values at the peak potentials, both anodic and cathodic, were analyzed with respect to the scan rate, which revealed a linear dependence with $v^{1/2}$. This behavior was indicative of a charge transfer process limited by a diffusional mass transport step, with the current at the peak potential, i_p, being related to the scan rate by the equation (at 25 °C) [16]:

$$i_p = (2.69 \times 10^5) A n^{3/2} C^* D^{1/2} v^{1/2} \quad (2)$$

where n is the number of electrons involved in the electrochemical reaction, considered as one electron for each Ti^{IV}, as the electrochemical reduction reaction of one Ti^{IV} center requires one Li^+ ion to be inserted in the solid matrix in order to compensate the charge balance in the solid LTO material without any stoichiometric changes

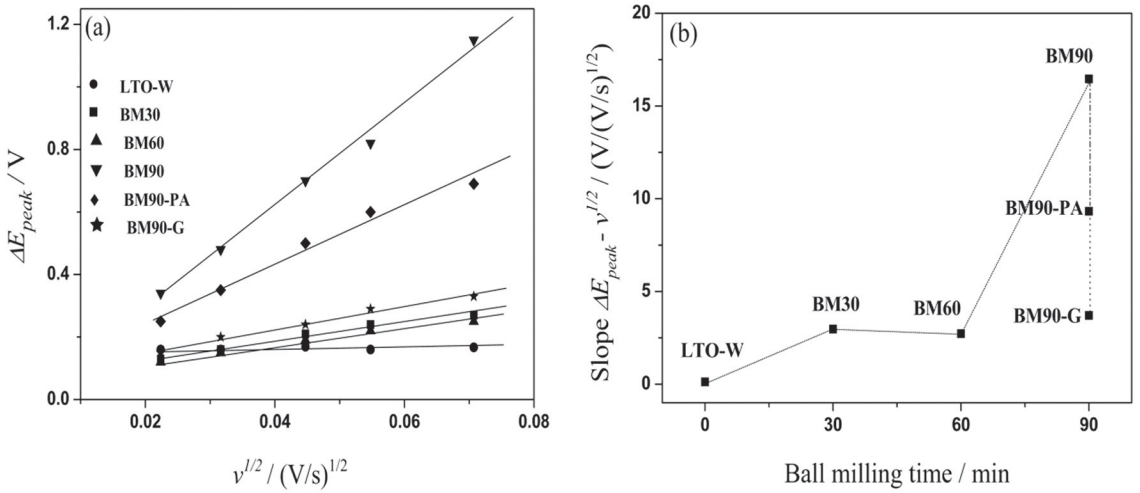


Fig. 9. (a) Dependence of the difference between the anodic and cathodic current peak potentials (ΔE_{peak}) with the square root of the scan rate ($v^{1/2}$) for all synthesized materials. (b) Slope of the ΔE_{peak} - $v^{1/2}$ graphic as a function of the ball milling time.

occurring in the titanium-to-oxygen relationship. *A* is the electrode area (in cm^2), *C** is the bulk concentration of Li^+ ions in the electrolyte (in mol/cm^3), *D* is its diffusion coefficient (in cm^2/s), and *v* is the potential scan rate (in V/s) in order to give i_p in amps.

Fig. A.2 in the Appendix displays the obtained linear relationship between i_p and $v^{1/2}$ for each electrode material studied and for both the anodic and cathodic processes. From the slope values of these graphics (with regression factors in the linear fit by the least square method between 0.950 and 0.999), the apparent diffusion coefficients of the lithium ions (D_{app}) in the LTO matrix were calculated (Table 2). Rather than being a true diffusion coefficient, the values of this parameter obtained represented the magnitude of the rate constant for the limiting mass transport process, thereby providing a comparison between the different synthesized materials. To calculate the diffusion coefficient value for each material, the total active mass deposited on the substrate and the particle size were taken into account, in order to obtain the total surface area exposed to solution by the particles in each case.

All these values are characteristic of an ion diffusion process into a solid matrix (the diffusion coefficients for ions in solution are around five to six orders of magnitude higher), and show interesting differences depending on the treatment of the LTO material. Fig. 10 displays these values as a function of the ball milling time, where it is possible to observe a moderate increase in the values for up to 30 min of ball milling, followed by a further decrease for 90 min. The calcination post ball milling for 90 min slightly increased the diffusion coefficient values, but the presence of graphite during the milling produced the highest values. It is important to mention here that this behavior is not a simple effect of the exposed surface areas of the different materials, because the diffusion coefficients were calculated considering the total surface of each material, but instead due to a high surface-to-volume (S/V) ratio together with a high state of crystallinity. The S/V effect prevailed in the LTO-W and BM30 samples, while the lack of crystallinity may have been the cause of the lower diffusion coefficient in the BM90 sample. In addition, the better results observed for the BM90-G sample might have been due to an optimal relationship occurring between these two features, along with another aspect that will be considered later.

From the observation of the current-potential profiles of the CV experiments, two other features can be described. First, the onset of the current peaks in the current-potential profiles, both cathodic and anodic and for all materials, showed a linear variation with the applied potential until almost reaching the peak potential. This aspect was markedly different from the usual voltammetric response of a redox couple in solution, and is characteristic of a redox process forming insoluble and resistive films on the electrode surface [17] or occurring in the solid phase. Other active materials used in batteries, such as PbO_2 in the cathode of the lead-acid battery, have shown a similar electrochemical CV behavior [18,19]. For the LTO materials obtained in the present work, the extension of a line drawn at the onset of one of the peaks coincided with that of the other peak, crossing the potential axis at zero current at about 1.55 V. This is very close to the value observed for the potential plateau of the GCD experiments, where this potential value is identified here as the equilibrium potential for the electrochemical Li^+ ion insertion reaction in the lithium titanate $Li_4Ti_5O_{12}$. The slope of this linear current-potential behavior ($\partial i/\partial V$) allows the resistive effect determining the *i-E* response at or near the equilibrium

Table 2
Apparent diffusion coefficients for the Li^+ ion in the cathodic and anodic processes (in cm^2/s), obtained from CV experiments. These values were calculated by considering the total surface area exposed to the solution, according to the particle size and deposited mass of each LTO material.

Sample	$D_{app}{}^{cath}$	$D_{app}{}^{an}$
LTO-W	4.21×10^{-12}	8.10×10^{-12}
BM30	2.02×10^{-11}	2.80×10^{-11}
BM60	1.14×10^{-11}	1.33×10^{-11}
BM90	1.57×10^{-12}	1.20×10^{-12}
BM90-PA	6.25×10^{-12}	1.71×10^{-11}
BM90-G	3.45×10^{-10}	3.31×10^{-10}

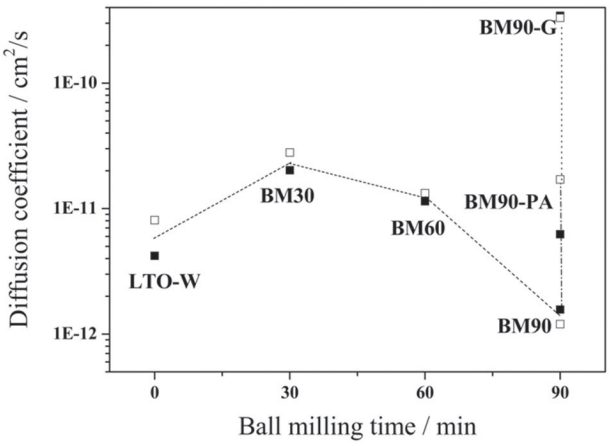


Fig. 10. Diffusion coefficient obtained from the i_p - $v^{1/2}$ plots in the CV experiments. Full symbol: diffusion coefficient obtained from the cathodic current peak $D_{app}{}^{cath}$; open symbol: diffusion coefficient obtained from the anodic current peak, $D_{app}{}^{an}$.

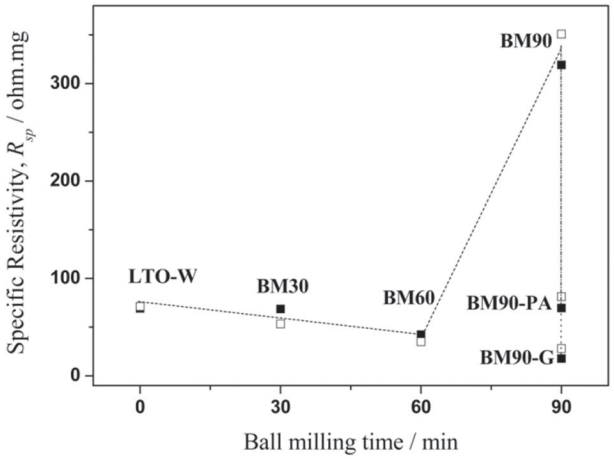


Fig. 11. Specific resistivity in terms of active mass, R_{sp} (ohm mg), obtained from the onset of the current peaks in the *j-E* profiles of the CV experiments (Fig. 7). Full symbol: value obtained from the onset of the cathodic current peak; open symbol: value obtained from the onset of the anodic current peak.

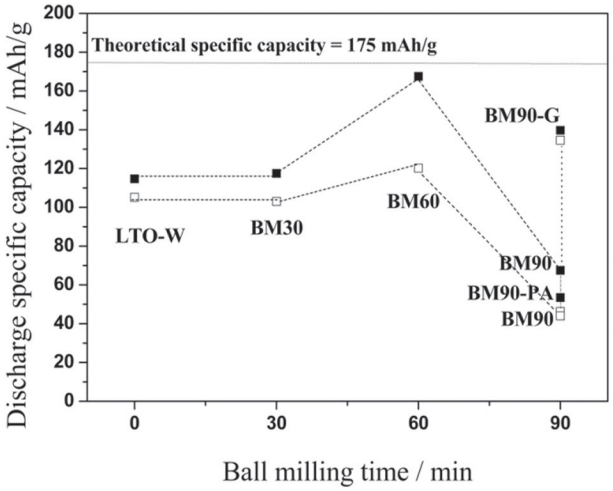


Fig. 13. Discharge specific capacity at 0.5 (full symbol) and 10C (open symbol) as a function of the ball milling time.

potential to be interpreted. The ($\partial i/\partial V$) values obtained from the CV curves for all materials, expressed as a specific resistivity in terms of active mass R_{sp} (ohm mg), are shown in Fig. 11 as a function of the ball milling time. Remarkably, the LTO-W, BM30, BM60 and BM90-PA materials had similar values of around 40–70 Ω mg, while the BM90 sample revealed the highest specific resistivity (about 319 Ω mg), in agreement with the loss in crystallinity of this material. In contrast, and not surprisingly, the presence of graphite in the milling process produced a LTO material with the highest electrical conductivity, as shown by its very low specific resistivity (17.8 Ω mg). Considering that the electrical properties of all these materials are based on that of titanium oxide TiO_2, which is well known by its semiconducting character, any strategy that can increase the conductivity (such as the doping with other metal atoms) but without a corresponding increase in mass of the unit formula (which leads to a reduction in the specific capacity) would be a remarkable achievement. It is important to note that in addition to the more conductive properties of BM90-G, this material showed a behavior similar to that of the quasi-reversible electrochemical kinetics found for the BM30 and BM60 samples, as described above (Fig. 9(b)). Thus, improved electrical properties of the materials are not directly correlated with a faster (or reversible) kinetic response.

Rate capability (RC) experiments were performed at a constant charge current of 0.5C and varying the discharge current (0.5, 1, 2, 5, 10 and 0.5C again), carrying out 10 cycles at each C rate in order to study the kinetics of the discharge process for all samples, with the results being shown in Fig. 12. Generally, all the responses appeared to be qualitatively similar, showing the expected behavior of an increase in the discharge current resulting in a reduction in the discharge capacity. However, all materials revealed a recovery in specific capacity to the initial values when the discharge rate was returned to 0.5C. The BM60 sample showed not only the highest discharge specific capacity values, but also the highest decay for each C rate applied consecutively. Comparatively, for the BM60 sample it was possible to extract at 10C (last cycle) only 71.8% of the charge extracted at 0.5C (first cycle), while for the other samples the extracted charge values ranged from 86 up to 91%. For BM90-G, a comparative charge/discharge experiment was also performed. In this case, the rate of the capacity decrease was the lowest, revealing 95.6% of the discharge specific capacity at 10C.

Fig. 13 shows the discharge specific capacity obtained at 0.5 (first cycle) and 10C (last cycle) as a function of the ball milling time. Here, an increase in specific capacity was again observed as the milling time increased for up to 60 min. This was followed by a sharp decrease between 60 and 90 min of ball milling time. The post-annealing treatment did not produce better results for a milling of 90 min, but the presence of graphite in the milling process greatly improved the performance, giving results similar to that of a 60 minute milling. In respect to experimental results reported in the literature over other LTO materials and/or the effect of different particle size, it is interesting to mention that S-B. Yoon et al. obtained 165 mAh/g for $Li_4Ti_5O_{12}$/reduced graphene oxide (LTO/RGO) nanocomposite and 117 mAh/g for commercial LTO, both measured at 0.4C [20] while L. Sun et al. using mesoporous LTO nanoclusters on C nanotubes have obtained 105 mAh/g at 0.58C [21], but Yu-S. Lin et al. obtained 140 mAh/g at 0.5C using also a mesoporous $Li_4Ti_5O_{12}$ [22]. On the other hand, G. Wang et al.

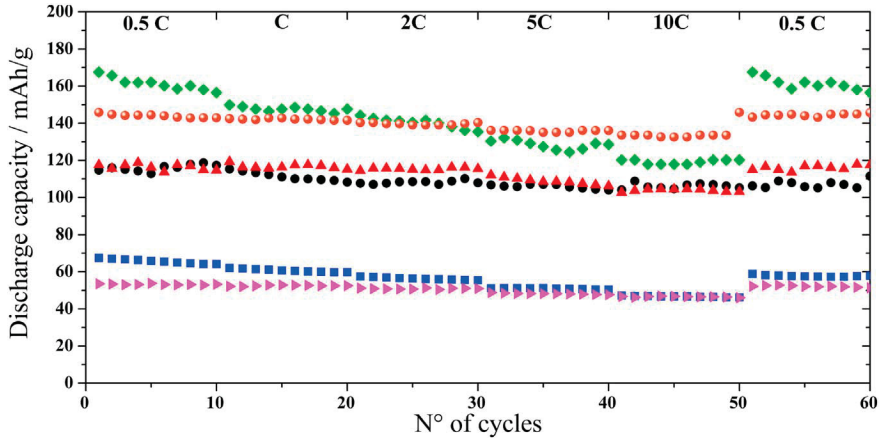


Fig. 12. RC experiments for all samples charged at constant current 0.5C and discharged at different consecutive rates: 0.5, 1, 2, 5, 10 and 0.5C. Reference: LTO-W (black circle), BM30 (red triangle), BM60 (green diamond), BM90 (blue square), BM90-PA (pink inverted triangle) and BM90-G (orange circle). (For interpretation of the references to colour in this figure legend, the reader is referred to the web version of this article.)

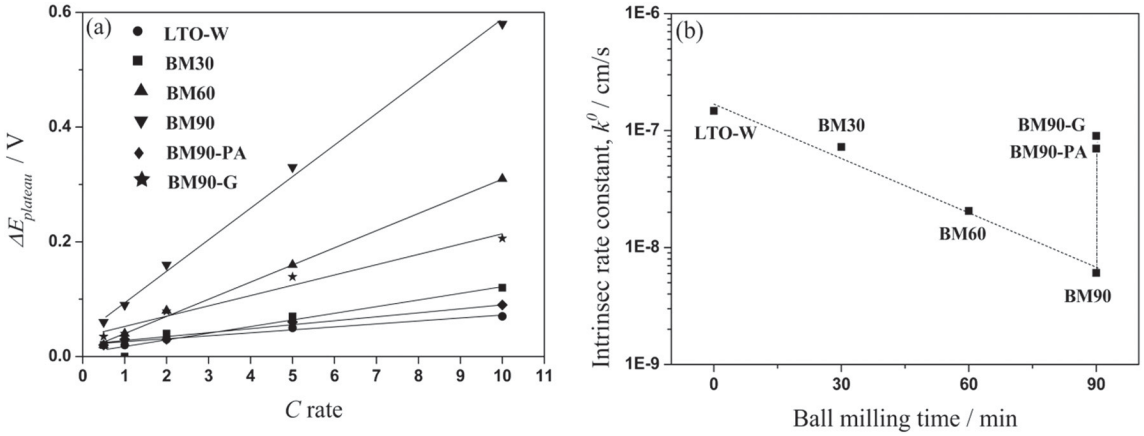


Fig. 14. (a) $\Delta E_{plateau}$ as a function of the *C* rate for all synthesized materials. (b) Intrinsic rate constant (k^0) values as a function of the ball milling time, for all synthesized materials.

sinthetized $Li_4Ti_5O_{12}$ powders with high energy ball milling, obtaining 146.9 mAh/g at 1C [23] while W. Liu et al. have prepared also $Li_4Ti_5O_{12}$ powders through high energy ball milling at different times, obtaining 131.4 and 137.2 mAh/g at 1C for a mean particle sizes of 0.757 and 0.594 μm, respectively [24]. Using a different preparation route, N. Zhang et al. have synthesized nanocrystalline $Li_4Ti_5O_{12}$ via sol–gel which yield 180 mAh/g at 1C [25]. K. Nakahara et al. prepared fine particulates of LTO with an average size of 0.7 μm giving 165 mAh/g at 1C, but bigger particles of 8.5 μm showed a decrease in capacity and lower rate capacity [26], However; K.-C. Hsiao et al. prepared porous (P-) and dense (D-) lithium titanate $Li_4Ti_5O_{12}$ powders having large particle size yet high specific capacity, having the P-LTO a particle size of 12 μm and specific capacity of 165 mAh/g while the D-LTO had 15 μm and 150 mAh/g, both measured at 0.2C [27].

As expected, the potential value of the plateau in the discharge cycle was greater at each increasing applied C rate (more positive values) with respect to the plateau potential at a charging cycle of 0.5C (figures not shown). Fig. 14(a) shows the shift between the potentials at which the charging and discharging plateaus are observed, calculated as $\Delta E_{plateau} = E_{plateau}{}^{C_i}, discharge - E_{plateau}{}^{0.5C,\,charge}$, as a function of the C rate, for all synthesized materials. In all cases, a linear increase was observed, with different slope values depending on the sample (the regression factors in the linear fit by the least square method were between 0.960 and 0.990). The linear responses indicated a resistive behavior being responsible for the shift in the plateau potential, which was a result of the applied increasing discharge current. These $\Delta E_{plateau}$ values can be considered to be a quasi-equilibrium (or steady state) overpotential, resulting from each applied *C* current. That is to say, $\Delta E_{plateau} \cong \eta(C)$, with η being directly proportional to the *C* current (or *i*). The slope of the $\Delta E_{plateau}$ vs *C* rate curves (translating the *C* to *i* values in amps) represents this experimental proportionality factor, which is in fact a resistance for the charge transfer process, R_{ct}, for each studied material.

Taking into account that the absolute *C* current values used were relatively low (from 40 to 120 μA, depending on the sample) and considering that the observed linear *i*-η relationship can be expressed through the linearized Butler-Volmer equation (valid in the low overpotential range), the relationship between current and overpotential can be written as $i = i_0\left({}^{nF}/_{RT}\right)\eta$ where i_0 is the exchange current for the present electrochemical process. This corresponds to the reduction of the Ti^{IV} centers during the charge process or to the oxidation of the Ti^{III} centers during the discharge process. Thus, for $n = 1$, the charge transfer resistance, R_{ct}, can be written as [28]:

$$R_{ct} = {}^{RT}\Big/_{Fi_0} \tag{3}$$

with the exchange current i_0 being expressed as:

$$i_0 = FAk^0C \tag{4}$$

This equation includes the surface area of the electrode *A* (the total exposed surface area of the particles, in cm^2), the concentration of the active species *C* (Li^+ ions in the electrolyte, in mol/cm^3), and the intrinsic rate constant, k^0, of the electrochemical reaction (in cm/s). The latter is an unknown parameter and allows us to characterize the kinetic aspects of the insertion/de-insertion of lithium ions in the different synthesized materials, which is given by:

$$k^0 = {}^{RT}\Big/_{AF^2CR_{ct}} \tag{5}$$

Table 3 shows the obtained values for k^0 for each electrode material, and in Fig. 13(b) k^0 is represented as a function of the ball milling time. The order of magnitude of these values (10^{-7}–10^{-9} cm/s) is typical for electrochemical processes occurring in a solid phase involving lithium ionic transport [29]. These values differ considerably from those found for usual charge transfer processes on metallic electrode surfaces from dissolved ions in solution (i.e. $Fe(CN)_6{}^{4-/3-}$ or $Fe^{2+/3+}$ on Pt electrodes), which range from 10^{-1}–10^{-3} cm/s [30].

There was a notable continuous decrease in the intrinsic rate constant with ball milling time, which showed a recovery when the higher milling time was followed by an annealing step or when it was synthesized with added graphite, resulting in these cases with values similar to those of the lower milling times. These results correlate well with those obtained in the cyclic voltammetry experiments from the variation in ΔE_{peak} with the square root of the scan rate. Thus, it is possible to conclude that while the specific capacity slightly improved with milling time, and then with the particle size reduction (except for the 90 minute sample), the kinetic response to the Li^+ insertion/de-insertion process was slightly worse. At first sight, this seems to be contradictory behavior, but in actual fact it is not. The experimental specific capacity exhibited by an electrode material depends on the accessibility degree of Li^+ ions at all available sites in the crystalline structure. This property is usually measured at low (or very low)

Table 3
Intrinsic rate constant values (k^0) obtained for each electrode materials from the slope of $\Delta E_{plateau}$ as a function of the applied *C* current (Fig. 13).

Sample	k^0/cm/s
LTO-W	1.47×10^{-7}
BM30	7.24×10^{-8}
BM60	2.06×10^{-8}
BM90	6.07×10^{-9}
BM90-PA	7.01×10^{-8}
BM90-G	9.01×10^{-8}

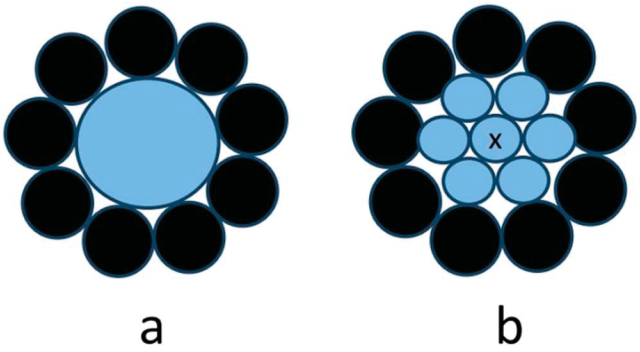


Fig. 15. Qualitative scheme to explain the loss of Li-ion storage capacity after extensive ball milling of the present LTO compounds. For a similar composition, we show a situation where the particles of the active material (blue) are relatively large (a) or relatively small (b) compared with the particles of the conductive particles (black). The particle marked with a cross is isolated from the conductive percolating network. (For interpretation of the references to colour in this figure legend, the reader is referred to the web version of this article.)

insertion rates (or currents). For low insertion rate conditions, the kinetic characteristics of the electrochemical process are not an important limiting aspect. Thus, we can assert that the high charge storage capacity for a given material does not necessarily correlate directly with the most favorable kinetic behavior. Thus, the search for a better active electrode material should be a compromise between these two relevant aspects.

It is interesting to analyze the present results in the light of modeling and recent computer simulations. Cerbelaud et al. [31] performed computational studies on the effects of the size of nanoparticles on the percolation properties of composites. This modeling aimed to achieve a better understanding of the Si-carbon black composites, but the results can also be extended to the present system. These authors used particles of different sizes to represent one side active materials, where lithium ion are incorporated and on the other side carbon black nanoparticles, which serve as electronic conductive materials, providing a network for the electrons to reach the active materials. Within this modeling, these authors were able to draw a number of interesting conclusions. Their results showed that, for a constant composition, decreasing the size of the active material particles (here the LTO particles) may be advantageous as this increases the number of contacts between the active material and the electronic network. However, the authors also pointed out that very small active particles can provoke the rupture of the percolating electronic network. In this context, Fig. 3 shows that the BM90 composite presented very small LTO particles that may be isolated from the percolating conductive network. This effect is illustrated qualitatively in Fig. 15, which compares a portion of two different systems having a similar composition but different particle sizes: one involving relatively large particles of the active material (Fig. 15(a)) and the other associated with small particles (Fig. 15(b)), with the figure showing qualitatively how one of the particles of the active material (marked with a cross) became isolated from the percolating conductive network. This type of loss of connectivity may have been responsible for the lowering of the Li-ion storage capacity observed on the blue line of Fig. 5(a).

4. Conclusions

In the present work, different electrochemical techniques were applied to study a lithium titanate compound ($Li_4Ti_5O_{12}$) synthesized by a solid-state and high temperature procedure, which was mechanically milled using a high-energy process (ball milling) at different times of up to 90 min in order to obtain progressively lower particle sizes. The particle size and crystallinity state were then measured. After 90 minute milling, a sample was annealed again at the same temperature as it was synthesized, in order to recover the loss in crystallinity state. Also, a sample was milled for the longest time in the presence of graphite particles, in order to obtain a hybrid lithium titanate compound.

For each applied electrochemical technique, different experimental parameters were obtained that were linked to several important properties of the material. From the GCD experiments, the specific capacity was determined, along with the stability towards the charge/discharge cycling. The Li-ion diffusion coefficient, D, for each material was obtained, as well as its specific resistivity and the changes in the intrinsic rate constant for the electrochemical process, k^0, from CV experiments at different scan rates. These parameters provided us with information about the limiting mass transport process, the internal resistance of the material to electronic/ionic conduction and the electrochemical kinetic as a function of the milling treatment. Finally, RC experiments yielded the specific capacity value of the discharge stage at different current values and also the k^0 values for each material, which revealed the discharge rate capability properties and enabled us to express in quantitative terms the electrochemical kinetic characteristics.

The application of high-energy milling at different times showed that the specific capacity increased with particle size reduction (a desired feature), as long as the crystallinity degree of the material remained high. The LTO material with the smallest particle size but with a poorly defined crystalline state demonstrated a lower specific capacity, with a similar behavior being observed for the diffusion coefficient and the specific resistivity. However, the k^0 value was found to reduce with a decrease in particle size and loss in degree of crystallinity. A post-annealing after 90 min of milling allowed a complete recovery of the degree of crystallinity, but produced a higher particle size due to synterization between small particles. This LTO material showed, in comparison with samples without annealing, better results for the D, R_{sp} and k^0 parameters (that is to say, better mass transport, a lower internal resistance and a higher electrochemical kinetic), but without any improvement in the charge storage capacity or in the discharge rate capability. The presence of graphite in the milling process at the longest time (90 min) produced a particle size greater than that of the corresponding process without graphite, and also showed an improvement in all the analyzed parameters (C_{sp}, D, R_{sp}, k^0 and discharge rate capability). When the LTO material was milled at 60 min, it almost reached the theoretical specific capacity for this material, with a high reversibility towards lithium ion insertion/de-insertion as well as an outstanding performance and robustness at high discharge current densities.

From the above results, it is possible to state that any treatment process on a given material that produces improvements in its charge storage capacity in parallel leads to improvements in mass transport and electrical conduction, although not necessarily implying better electrochemical kinetic behavior. An optimal post-treatment requires the management of particle size, crystallinity and the inter-particle conductivity. In the present study, optimal milling conditions have been interpreted in terms of recent modeling reported in the literature, where decreasing the particle size of the active material seems advantageous due to the increase in the number of contacts with the electronic network, but also very small active particles could modify the percolating electronic network and be isolated from the electrical connection to the current collector.

Acknowledgments

This work was supported by PID 2011-0070, Program BID (PICT-2011-0754, 2012-2324), SeCyT of the Universidad Nacional de Córdoba(103/15) and YPF-Tecnología (Y-TEC)(2013/2015 and 2015/2016), Argentina. S. Chauque wishes to thank CONICET for the doctoral fellowship. This work was performed at INFIQC-CONICET and Facultad de Ciencias Químicas-Universidad Nacional de Córdoba, Argentina.

Appendix A

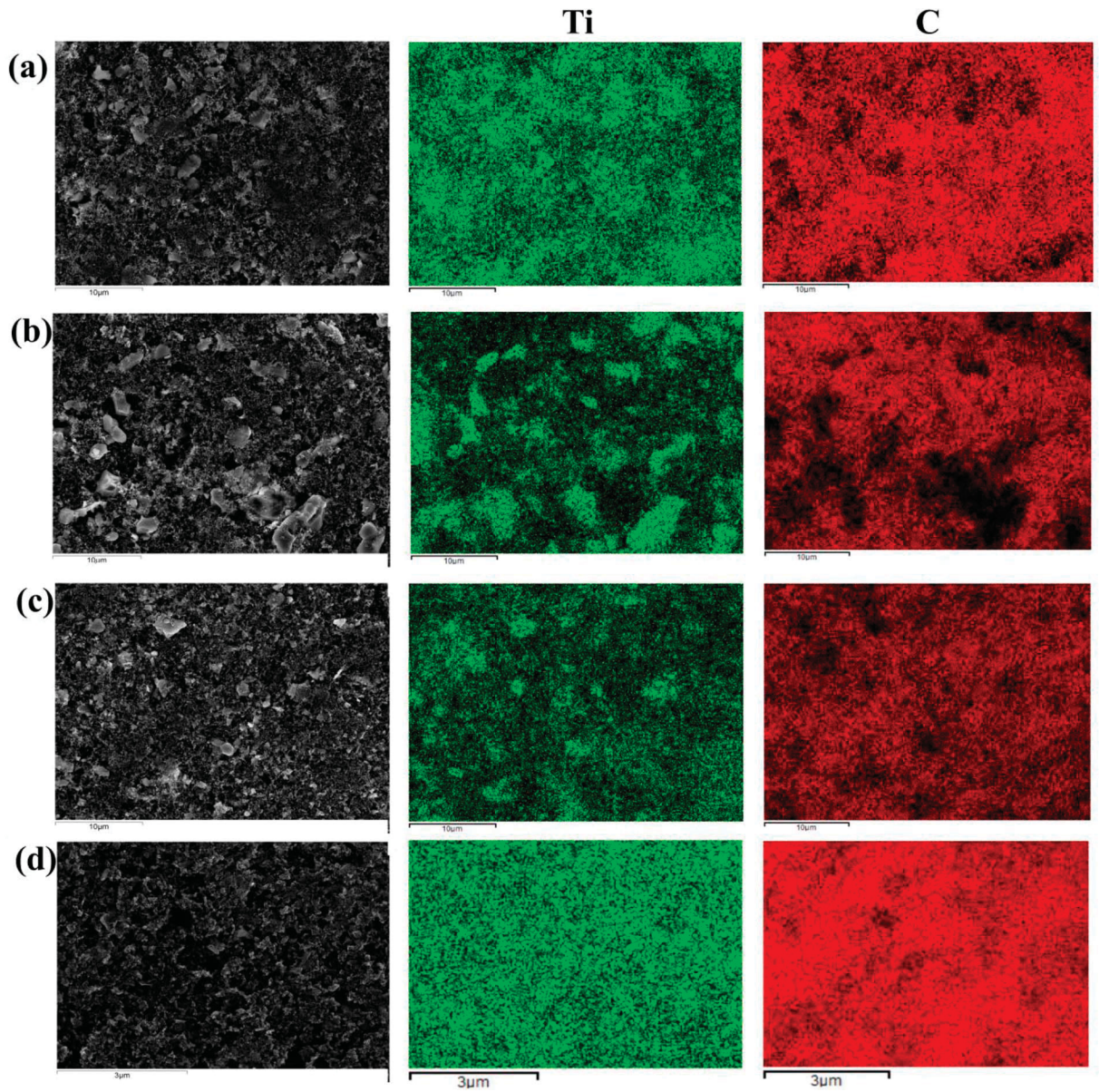


Fig. A.1. SEM micrographs and titanium (green) and carbon (red) distribution (first, second and third column, respectively) corresponding to the surface of: (a) LTO-W, (b) BM30, (c) BM60, and (d) BM90 electrodes. The titanium and carbon content was obtained by Electron Probe Micro-Analysis (EPMA).

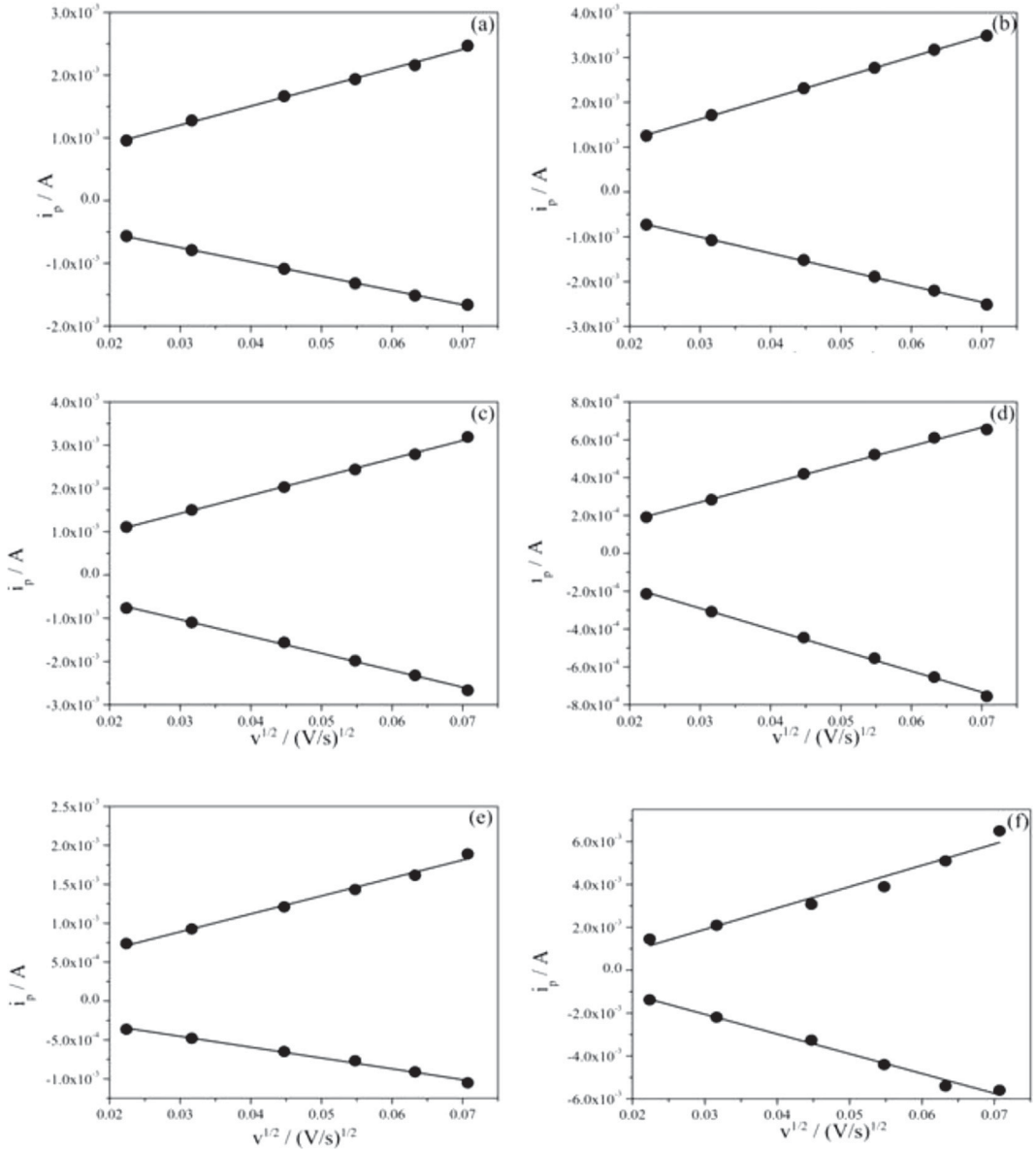


Fig. A.2. Dependence between the anodic (positive data points) and cathodic (negative data points) peak currents vs. the square root of the scan rate, corresponding to (a) LTO-W, (b) BM30, (c) BM60, (d) BM90, (e) BM90-PA and (f) BM90-G.

References

[1] M. Armand, J.M. Tarascon, Building better batteries, Nature 451 (2008) 652.
[2] C.B. Robledo, M. Otero, G. Luque, O. Cámara, D. Barraco, M.I. Rojas, E.P.M. Leiva, First-principles studies of lithium storage in reduced graphite oxide, Electrochim. Acta 140 (2014) 232.
[3] C.B. Robledo, J.E. Thomas, G. Luque, E.P.M. Leiva, O. Cámara, D. Barraco, A. Visintin, An experimental and theoretical approach on the effect of presence of oxygen in milled graphite as lithium storage material, Electrochim. Acta 140 (2014) 160.
[4] C.P. Sandhya, B. John, C. Gouri, Lithium titanate as anode material for lithium-ion cells: a review, Ionics 20 (2014) 601.
[5] M.N. Thackeray, From gems to lithium battery electrodes: the significance of the diamond, ruby (sapphire), spinel and peridot structures, J. Power Sources 97-98 (2001) 1.
[6] T. Yuan, X. Yu, R. Cai, Y. Zhou, Z. Shao, Synthesis of pristine and carbon-coated $Li_4Ti_5O_{12}$ and their low-temperature electrochemical performance, J. Power Sources 195 (2010) 4997.
[7] H. Zhang, et al., Electrochemical lithium storage of titanate and titania nanotubes and nanorods, J. Phys. Chem. B 111 (2007) 6143.
[8] A.R. Armstrong, G. Armstrong, J. Canales, P.G. Bruce, TiO_2-B nanowires as negative electrodes for rechargeable lithium batteries, J. Power Sources 146 (2005) 501.
[9] D.P. Singh, F.M. Mulder, M. Wagemaker, Templated spinel $Li_4Ti_5O_{12}$ Li-ion battery electrodes combining high rates with high energy density, Electrochem. Commun. 35 (2013) 124.
[10] W.-H. Ryu, D.-H. Nam, Y.-S. Ko, R.-H. Kim, H.-S. Kwon, Electrochemical performance of a smooth and highly ordered TiO_2 nanotube electrode for Li-ion batteries, Electrochim. Acta 61 (2012) 19.
[11] S. Huang, Z. Wen, Z. Gu, X. Zhu, Preparation and cycling performance of Al^{3+} and F^- co-substituted compounds $Li_4Al_xTi_{5-x}F_yO_{12-y}$, Electrochim. Acta 50 (2005) 4057.
[12] S. Chauque, C.B. Robledo, E.P.M. Leiva, F.Y. Oliva, O.R. Camara, Comparative study of different alkali (Na, Li) titanate substrates as active materials for anodes of lithium ion batteries, ECS Trans. 63 (1) (2014) 113.
[13] X. Sun, P.V. Radovanovic, B. Cui, Advances in spinel $Li_4Ti_5O_{12}$ anode materials for lithium-ion batteries, New J. Chem. 39 (2015) 38.
[14] J. Shu, Electrochemical behavior and stability of $Li_4Ti_5O_{12}$ in a broad voltage window, J. Solid State Electrochem. 13 (2009) 1535.
[15] H. Ge, N. Li, D. Li, C. Dai, D. Wang, Study on the theoretical capacity of spinel lithium titanate induced by low-potential intercalation, J. Phys. Chem. C 113 (2009) 6324.
[16] A.J. Bard, L.R. Faulkner, Electrochemical Methods. Fundamentals and Applications, second ed., John Wiley & Sons, Inc., New York, 2001 (Ch. 6).
[17] A.J. Calandra, N.R. de Tacconi, R. Pereiro, A.J. Arvia, Potentiodynamic current/potential relations for film formation under OHMIC resistance control, Electrochim. Acta 19 (1974) 901.
[18] A. Hazza, D. Pletcher, R. Wills, A novel flow battery: a lead acid battery based on an electrolyte with soluble lead(II). Part I. Preliminary studies, Phys. Chem. Chem. Phys. 6 (2004) 1773.
[19] X. Li, D. Pletcher, F.C. Walsh, A novel flow battery: a lead acid battery based on an electrolyte with soluble lead(II): Part VII. Further studies of the lead dioxide positive electrode, Electrochim. Acta 54 (2009) 4688.
[20] Seung-Beom Yoon, Hyun-Kyung Kim, Kwang Chul Roh, Kwang-Bum Kim, Electrochemical kinetics investigation of $Li_4Ti_5O_{12}$/reduced graphene oxide nanocomposite using voltammetric charge analysis, J. Electrochem. Soc. 162 (2015) A667.
[21] Li Sun, Weibang Kong, Hengcai Wu, Yang Wu, Datao Wang, Fei Zhao, Kaili Jiang, Qunqing Li, Jiaping Wang, Shoushan Fan, Mesoporous $Li_4Ti_5O_{12}$ nanoclusters anchored on super-aligned carbon nanotubes as high performance electrodes for lithium ion batteries, Nano 8 (2016) 617.
[22] Yu-Sheng Lin, Jenq-Gong Duh, Facile synthesis of mesoporous lithium titanate spheres for high rate lithium-ion batteries, J. Power Sources 196 (2011) 10698.
[23] Guixin Wang, Jingjing Xu, Ming Wen, Rui Cai, Ran Ran, Zongping Shao, Influence of high-energy ball milling of precursor on the morphology and electrochemical performance of $Li_4Ti_5O_{12}$–ball-milling time, Solid State Ionics 179 (2008) 946.
[24] Wei Liu, Jian Zhang, Qian Wang, Xiaohua Xie, Yuwan Lou, Xuewu Han, Baojia Xia, Microsized TiO_2 activated by high-energy ball milling as starting material for the preparation of $Li_4Ti_5O_{12}$ anode material, Powder Technol. 247 (2013) 204.
[25] Naiqing Zhang, Zhimin Liu, Tongyong Yang, Chenglong Liao, Zhijun Wang, Kening Sun, Facile preparation of nanocrystalline $Li_4Ti_5O_{12}$ and its high electrochemical performance as anode material for lithium-ion batteries, Electrochem. Commun. 13 (2011) 654.
[26] Kiyoshi Nakahara, Ryosuke Nakajima, Tomoko Matsushima, Hiroshi Majima, Preparation of particulate $Li_4Ti_5O_{12}$ having excellent characteristics as an electrode active material for power storage cells, J. Power Sources 117 (2003) 131.
[27] Kuang-Che Hsiao, Shih-Chieh Liao, Jin-Ming Chen, Microstructure effect on the electrochemical property of $Li_4Ti_5O_{12}$ as an anode material for lithium-ion batteries, Electrochim. Acta 53 (2008) 7242.
[28] H. Ge, N. Li, D. Li, C. Dai, D. Wang, Study on the theoretical capacity of spinel lithium titanate induced by low-potential intercalation, J. Phys. Chem. C 113 (2009) 6324.
[29] M.D. Levi, G. Salitra, B. Markovsky, H. Teller, D. Aurbach, U. Heider, L. Heider, Solid-state electrochemical kinetics of Li-ion intercalation into $Li_{1-x}CoO_2$: simultaneous application of electroanalytical techniques SSCV, PITT, and EIS, J. Electrochem. Soc. 146 (1999) 1279.
[30] R.A. Marcus, On the theory of oxidation-reduction reactions involving electron transfer. V. Comparison and properties of electrochemical and chemical rate constants, J. Phys. Chem. 67 (1963) 853.
[31] M. Cerbelaud, B. Lestriez, A. Videcoq, R. Ferrando, D. Guyomard, Understanding the structure of electrodes in Li-ion batteries: a numerical study, J. Electrochem. Soc. 162 (2015) A1485.